Thermal Coherence Tomography Using Match Filter Binary Phase Coded Diffusion Waves

Nima Tabatabaei and Andreas Mandelis*

Center for Advanced Diffusion-Wave Technologies (CADIFT), Department of Mechanical and Industrial Engineering, University of Toronto, Toronto, Ontario, M5S 3G8, Canada

(Received 10 June 2011; revised manuscript received 8 August 2011; published 10 October 2011)

Energy transport in diffusion-wave fields is gradient-driven and therefore diffuse, yielding depth-integrated responses with poor axial resolution. Using matched-filter principles, we propose a methodology enabling these parabolic diffusion-wave energy fields to exhibit energy localization akin to propagating hyperbolic wave fields. This not only improves axial resolution but also allows for deconvolution of individual responses of superposed axially discrete sources, opening a new field of depth-resolved subsurface thermal coherence tomography using diffusion waves.

DOI: 10.1103/PhysRevLett.107.165901 PACS numbers: 66.10.cd, 07.05.Pj, 78.20.nd, 87.57.−s

Diffusion-wave science has received much attention in recent years, spanning from thermal waves [1] to carrier plasma diffusion waves, diffuse photon density waves, and mass-transport waves [2]. One interesting case of diffusive waves is that of thermal waves. Unlike hyperbolic traveling waves such as acoustic or optical waves, the physics of diffusive thermal waves is governed by the parabolic heat diffusion equation and in accordance to Fickian principles. An immediate consequence of the gradient-driven principle is the lack of wave fronts and the diffuse depth-integrated (rather than localized) transport of power through the medium, leading to poor diffusive axial resolution. This diffusive limitation has tempted several researchers to treat the frequency-domain heat diffusion equation as a hyperbolic Helmholtz equation with a complex wave number, defining wave fronts and applying Snell's refraction laws to thermal waves [3]. Others adopted the hyperbolic Cattaneo-Vernotte relativistic heat conduction equation from step one [4]. While these interpretations seem to allow for wave fronts leading to depth-selective transfer of power by thermal waves, they both violate the second law of thermodynamics as they admit the propagation of energy against the field gradient (i.e., a temperature field in which heat would appear to be moving from cold to hot) [5]. The intention of this Letter is to show how nonpropagating (parabolic) diffusion-wave energy fields can exhibit energy localization normally encountered in propagating hyperbolic wave fields through a new thermal-wave binary phase code generation scheme and the subsequent matched-filter signal processing using the parabolic diffusion-wave equation. Such localized response from a diffusion wave not only results in an improvement in axial resolution for thermal-wave imaging but also allows the deconvolution of individual responses of superposed axially discrete sources and leads to depth-selective rather than depth-integrated images. These concepts are not limited to thermal waves but are of very broad interest to all parabolic diffusion-wave fields.

Cross correlation (CC) matched filtering was introduced in the radar sciences in the early 1940s to detect deterministic signals within highly noised channels and to augment range resolution. This methodology localizes the energy of the received signal under a single peak located at a delay time (τ_p) equal to the delay between the transmitted and received signals. More energy localization can be achieved by means of pulse compression techniques such as frequency chirp or binary phase coded (BPC) modulation through reducing the width of the CC peak while increasing its height.

While the frequency chirp modulation maintains a relatively constant power within the chirp frequency range (wideband detection), BPC modulation results in distinct energy localization advantages, especially with diffusive fields. A comprehensive study on BPC can be found in Ref. [6]. The codes introduced in Ref. [7] have been modified to minimize sidelobes and used in our experiments. The BPC signal $f(t)$ consists of a single frequency carrier $C(t)$ and a binary coded envelope $E(t)$. The signal is formed either by multiplying these components in the time domain or alternatively by convolving their spectra in the frequency domain. In general, an arbitrary binary sequence can be defined as $a_j = [a_1, a_2, \ldots, a_N]$. In the special case where the temporal length of each code element equals the period of the carrier (T_0), the binary coded envelope can be modeled as a series of rectangular pulses of width T_0 and height a_j shifted in the time axis by $(j - 0.5)T_0$. Therefore, starting with the Fourier transform of a pulse, the analytical spectrum of the binary coded envelope can be obtained by using the time-frequency shifting property of the Fourier transform:

$$\Im\{E(t)\} = E(\omega) = \frac{\sqrt{2\pi}}{\omega_o}\,\mathrm{sinc}\left(\frac{\omega}{\omega_o}\right) \times \sum_{j=1}^{N} a_j \exp[-i\omega T_0(j - 0.5)], \quad (1)$$

where ω_o and i are the carrier angular frequency and the imaginary unit, respectively. Finally, the analytical spectrum of the binary phase coded signal can be calculated

through the convolution of Eq. (1) and the spectrum of the carrier waveform:

$$\Im\{f(t)\} = F(\omega) = \frac{\pi}{i\omega_o} \times \sum_{j=1}^{N} \left[\begin{array}{l} a_j \operatorname{sinc}\left(\frac{\omega-\omega_o}{\omega_o}\right) \exp[-iT_0(j-0.5)(\omega-\omega_o)] \\ -a_j \operatorname{sinc}\left(\frac{\omega+\omega_o}{\omega_o}\right) \exp[-iT_0(j-0.5)(\omega+\omega_o)] \end{array} \right]. \quad (2)$$

Equation (2) suggests that the spectrum of the binary coded signal consists of a series of weighted "sinc" functions yielding a narrow-band waveform with most of its energy located at the carrier frequency (narrow-band signal).

The thermophotonic response (Planck radiation emission) of a nonopaque turbid medium to a BPC excitation can be obtained through coupling of the optical- and thermal-wave fields, where the total optical field (coherent + scattered) is the source of thermal-wave generation. As an important biophysics application, this Letter analytically investigates the response of blackbody absorbers in a turbid medium. That is, the BPC excitation is applied to the surface ($z = 0$) of a turbid medium with known scattering and absorption coefficients (μ_s and μ_a, respectively), where, after interaction with the turbid medium, the attenuated light is completely absorbed at $z = l$ and thermal waves are generated. The thermal-wave problem can be formulated by adding a depth-dependent source term to the heat diffusion differential equation (due to absorption by the medium) as well as an attenuated heat source at $z = l$ through a boundary condition:

$$\begin{aligned} &\frac{\partial^2\theta(z;\omega)}{\partial z^2} - \sigma^2\theta(z;\omega) = -\frac{\mu_a}{k} I(z) F(\boldsymbol{\omega}), \\ &-k\frac{\partial\theta(z;\omega)}{\partial z}\bigg|_{z=0} = 0 \quad \text{(I)}, \\ &-k\frac{\partial\theta(z;\omega)}{\partial z}\bigg|_{z=l} = I(l)F(\omega) \quad \text{(II)}, \\ &\theta(z;\omega) = \Im\{T(z,t) - T_\infty\}, \end{aligned} \quad (3)$$

where k, α, and $F(\omega)$ are thermal conductivity, thermal diffusivity, and the spectrum of the applied BPC excitation (2), respectively, and $\sigma = \sqrt{i\omega/\alpha}$ is the complex wave number. The energy fluence $I(z = l)$ of the one-dimensional, uniform, collimated beam normally incident on a homogeneous scattering and absorbing medium has been calculated by Prahl, Vitkin, and Bruggemann [8]. Note the similarity of (3) to the Helmholtz equation of hyperbolic wave fields. By solving the frequency-domain differential equation subject to the boundary conditions (I) and (II) and considering an average value for the infrared absorption coefficient within the spectral range of the detector ($\bar{\mu}_{\mathrm{IR}}$), the conductive heat transfer spectrum of the thermophotonic signal can be calculated as

$$\begin{aligned} S_c(l;\omega) &\propto \bar{\mu}_{\mathrm{IR}} \int_0^l \theta(z;\omega)\exp(-\bar{\mu}_{\mathrm{IR}} z)dz \\ &= \bar{\mu}_{\mathrm{IR}} \left[\begin{array}{l} \frac{A}{\sigma-\bar{\mu}_{\mathrm{IR}}}\{\exp[(\sigma-\bar{\mu}_{\mathrm{IR}})l]-1\} - \frac{B}{\sigma+\bar{\mu}_{\mathrm{IR}}}\{\exp[-(\sigma+\bar{\mu}_{\mathrm{IR}})l]-1\} \\ -\frac{C}{\mu_{\mathrm{eff}}+\bar{\mu}_{\mathrm{IR}}}\{\exp[-(\mu_{\mathrm{eff}}+\bar{\mu}_{\mathrm{IR}})l]-1\} - \frac{D}{\mu_t+\bar{\mu}_{\mathrm{IR}}}\{\exp[-(\mu_t+\bar{\mu}_{\mathrm{IR}})l]-1\} \end{array} \right], \end{aligned} \quad (4)$$

where $\mu_{\mathrm{eff}} = \sqrt{3\mu_t\mu_a}$, $\mu_t = \mu_a + \mu_s'$, $\mu_s' = \mu_s(1-g)$, and g is the average cosine of the scattering angle. However, the infrared emission captured by the detector is the superposition of (4) and the direct Planck emission from the blackbody absorber, attenuated through the turbid medium:

$$S(l;\omega) \propto S_c(l;\omega) + \theta(l;\omega)\exp(-\bar{\mu}_{\mathrm{IR}} l). \quad (5)$$

Equations (2) and (5) formulate the spectra of the applied binary phase coded excitation (i.e., the matched filter) and the thermophotonic response of a subsurface absorber at depth l to such excitation, respectively. Consequently, one can calculate the matched-filter cross-correlation signal and its phase analytically as (6a) and (6b), respectively, or experimentally via the algorithm depicted in Fig. 1(a):

$$\mathrm{CC}(l;\tau) = \varepsilon \times \Im^{-1}\{F(\omega)^* S(l;\omega)\}, \quad (6a)$$

$$\theta_{\mathrm{CC}}(l) = \frac{\not\in \times \Im^{-1}\{F(\omega)^* S(l;\omega)\}}{\not\in \times \Im^{-1}\{[-i\,\mathrm{sgn}(\omega)F(\omega)]^* S(l;\omega)\}}\bigg|_{\tau=0}, \quad (6b)$$

where $\mathrm{sgn}(\omega)$ is the signum function and the expression inside the square bracket in the denominator is the Fourier transform of the quadrature reference signal, experimentally obtained through the Hilbert and then Fourier transforms as shown in Fig. 1(a).

Figure 1(b) plots the theoretical CC phase of two extreme $\bar{\mu}_{\mathrm{IR}}$ cases for a 7-bit binary code as a function of the subsurface absorber depth l at several carrier frequencies. In both $\bar{\mu}_{\mathrm{IR}}$ cases, at a given carrier frequency, the deeper the absorber, the larger the amount of phase shift, showing a more delayed contribution from the deeper absorber. Moreover, an increase in the carrier frequency reduces the maximum probing depth due to the reduced thermal diffusion length [1], as expected. The key point in this

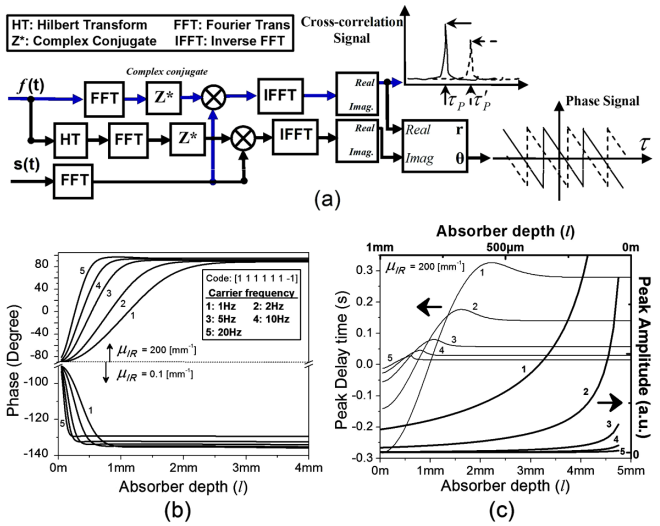

FIG. 1 (color online). (a) BPC imaging signal processing algorithm. Theoretical cross-correlation (b) phase, (c) peak delay time (left and bottom axis), and amplitude (right and top axis) curves as a function of the subsurface absorber depth using properties of dental enamel: $\mu_a = 100\ [\mathrm{m}^{-1}]$, $\mu_s = 6000\ [\mathrm{m}^{-1}]$, $g = 0.96$, $r = 0.65$, $k = 0.9\ [\mathrm{W m}^{-1}\,\mathrm{k}^{-1}]$, and $\alpha = 5 \times 10^{-7}\ [\mathrm{m}^2\,\mathrm{s}^{-1}]$. The numbers accompanying the curves determine the carrier frequency according to the inset of part (b).

figure is the effect of $\bar{\mu}_{\mathrm{IR}}$. The infrared radiation captured by the detector is composed of a delayed conductive thermal-wave portion and an instantaneous direct Planck emission [Eq. (5)]. While an increase in the direct emission improves the signal-to-noise ratio of the amplitude channel, it deteriorates the maximum probing depth of the phase channel. This happens because the direct emissions from absorbers at different depths are instantaneous and therefore all in phase, dominating the depth-dependent phase information of the conductive portion and consequently limiting the maximum probing depth [Fig. 1(b)]. Figure 1(c) shows how the height (peak amplitude channel) and location (peak delay time channel) of the CC signal peak behaves as a function of absorber depth at various carrier frequencies. Generally, a shallower absorber results in a higher amplitude and shifts the CC peak location to shorter delay times to manifest a less attenuated thermal-wave source closer to the interrogated surface. In other words, matched filtering in diffusion-wave fields acts as constructive interferometry, localizing the energy of the long-duty BPC excitation under a narrow peak whose location on the delay time axis is linked to the depth of the source and allows one to construct isodelay or alternatively isodepth (depth-selective) images. This is the diffusion equivalent of optical coherence tomography. For thermal waves, while the amplitude channel has by far the highest signal-to-noise ratio, it is less reliable because, unlike phase and peak delay time, it is not an emissivity-normalized quantity. An important feature of BPC imaging is the effect of code length. While increasing the code length does not alter the CC phase and peak delay time curves of Fig. 1, it increases the pulse compression ratio, i.e., increases the amplitude of the CC peaks and signal-to-noise ratio.

In order to demonstrate depth selectivity in broad classes of materials, from tissue phantoms to metals, an experimental setup was built by using a continuous-wave fiber-coupled 808-nm near-infrared laser illuminating the sample (JENOPTIK, Germany), a midinfrared camera focused on the interrogated surface of the sample (Cedip Titanium 520 M, France, spectral range of 3.6–5.1 μm and frame rate of 370 Hz), a signal generation and acquisition device (National Instruments NI-6229 BNC), and a 4-axis sample positioning system [9]. The laser power was modulated sinusoidally by the signal generation device either at a fixed frequency [conventional lock-in thermography (LIT)] or in a binary phase coded manner (BPC imaging) to generate photothermal waves inside the sample. The data acquisition and signal processing program (designed in a LABVIEW environment) captures and averages the camera frames and their corresponding reference (modulation) signal values. In the case of LIT, a standard 2D quadrature demodulation was used to determine the amplitude and phase values of the thermal waves generated inside the sample [10]. For the case of BPC imaging, based on (6a) and (6b), the temporal infrared signal corresponding to each pixel, $s(t)$, was cross correlated once with the reference (modulation) signal $f(t)$ and once with its quadrature. Subsequently, the CC and phase signals were calculated [Fig. 1(a)].

Depending on the contrast parameter chosen (the peak amplitude or its corresponding delay time τ_p), two kinds of images can be produced from the CC signal: an amplitude image or a peak delay time τ_p image, respectively. Moreover, based on Eq. (6b) it is also possible to calculate the emissivity-normalized CC phase images. Figure 2(a) schematically shows the cross section of a black plastic step wedge sample (step height = 200 μm) inside a tissue mimicking scattering medium (polyvinyl chloride-plastisol with added titanium dioxide TiO_2 powder to enhance scattering [11]). Figure 2(b) shows the conventional LI phase image obtained at 3 Hz along with its mean profile over the steps. It can be seen that, although LI imaging can detect all the steps, it loses its depth resolution over deeper steps due to the diffuse nature of thermal waves. On the other hand, BPC imaging at the same modulation frequency and experimental conditions (averaging, laser power, etc.) maintains excellent resolution down to the deepest step in both peak delay time and phase images [Figs. 2(c) and 2(d), respectively]. This experiment clearly shows how BPC matched filtering can result in a localized response in a diffusive field and improve the axial resolution while probing deeply into the sample.

Figure 3 demonstrates the principle of thermal coherence tomography (TCT) experimentally. It involves

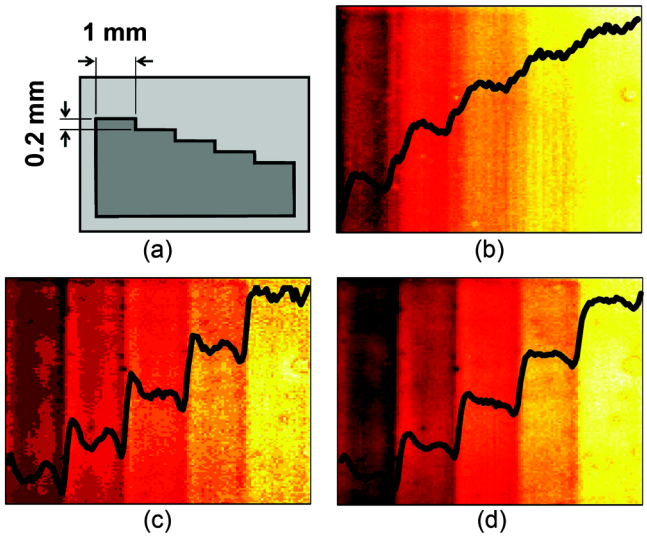

FIG. 2 (color online). (a) Cross section of the step wedge sample. (b) Conventional LIT phase, (c) BPC peak delay time, and (d) BPC phase images of the step wedge sample using 16-bit code at 3 Hz (acquisition time = 5.33 s). The curve in each image shows the mean horizontal profile of the corresponding contrast parameter.

a well-known limitation and challenge of diffusion fields: resolving stacked overlapping defects. Figure 3(a) shows an exploded view of a cross-shaped sample made of two strip absorbers. The deeper strip is a black plastic sample completely absorbing the optical flux, while the shallower strip is a partially absorbing phantom. All other components are transparent polyvinyl chloride-plastisol.

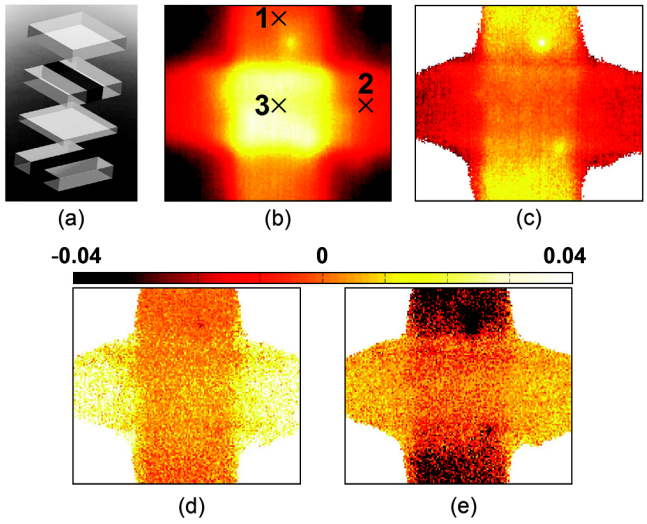

FIG. 3 (color online). (a) Exploded view of the cross-shaped sample with two absorbers at different depths. Conventional LIT (b) amplitude and (c) phase image. TCT peak delay time image matched to the camera temporal data of (d) point 1 and (e) point 2, as indicated in part (b), using a 3-bit [1 1 −1] code at 1 Hz (acquisition time = 3 s).

When viewed from the top, the cross sample covers all possible combinations: absorbers at two different depths [the end sections of the absorbing strips, points 1 and 2 in Fig. 3(b)] and two absorbers on top of each other [point 3 in Fig. 3(b)]. Figures 3(b) and 3(c) show the conventional lock-in amplitude and phase images of this sample, respectively. The amplitude image cannot distinguish between the deeper and shallower absorbers (vertical and horizontal strip, respectively). However, the amplitude information can be used to extract and process only those pixels having a high value (i.e., a subsurface absorber). Although the lock-in phase image yields significantly different values over the single absorbers (points 1 and 2), it cannot detect the layered structure of point 3. The axial resolution of both amplitude and phase images is limited by the depth-integrated nature of thermal waves.

Figures 3(d) and 3(e) are the BPC peak delay time images using the temporal data of points 1 and 2 as the matched filter, respectively. When using the temporal camera data of point 1 as the matched filter, all the diffusion waves originating at the same depth as that of point 1 will have their CC peaks located at $\tau = 0$. A similar situation arises in Fig. 3(e) for thermal waves from the shallower absorber using the temporal camera data of point 2 as the matched filter. The fact that the layered structure of point 3 exhibits a maximum correlation to both data of points 1 and 2 ($\tau_p = 0$) acting as the reference arm of a Michelson interferometer shows that matched-filter BPC imaging can resolve the layered structure axially. This depth-resolved phenomenon is normally a property of propagating hyperbolic wave fields and not of parabolic (diffusive) fields. The implications of BPC imaging with a delay-adjustable CC reference peak (TCT) can open a new field of generating layer-by-layer subsurface thermo-optic imaging at several millimeter-depth ranges (thermal coherence length) in wide ranges of solid and liquid matter, using naturally incoherent diffusion waves.

Two illustrations of the broad capabilities of this TCT imaging modality involve biological tissue and metals with defects. TCT has the ability to detect early caries in human teeth which conventional clinical diagnostic modalities, like x rays, cannot detect [9]. Early caries remove mineral from areas very close to the enamel surface and create light-trapping micropores, promoting close-to-surface light absorption and thermal-wave generation. However, dental thermophotonic lock-in imaging is unable to detect early interproximal (in between teeth) caries when inspected from the accessible buccal (front) surface, as the response is dominated by the thick healthy underlayers due to the depth-integrated nature of thermal waves. A comparison of LIT and TCT phase images of Figs. 4(b) and 4(c) under identical experimental conditions shows how the enhanced axial resolution of the depth-selective TCT imaging can resolve deep interproximal caries. Nondestructive evaluation of metallic and industrial samples is at the other

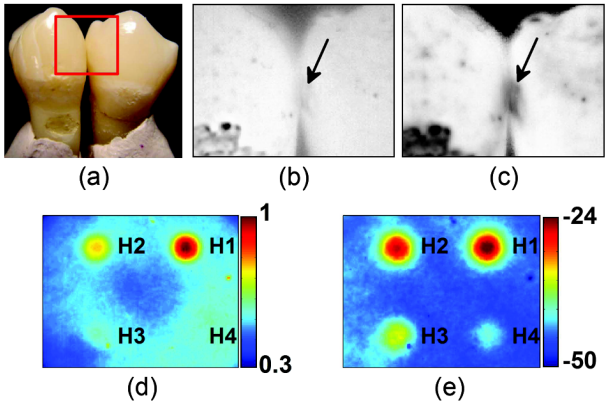

FIG. 4 (color online). (a) Teeth matrix with hidden interproximal early caries. The rectangle shows the imaged area. (b) Conventional LIT and (c) TCT phase images of the teeth matrix. TCT (d) amplitude and (e) phase images of an AISI 1010 steel block with blind holes $H1 = 0.4$, $H2 = 0.6$, $H3 = 1$, and $H4 = 1.5$ mm below the surface using a 16-bit code at 2 Hz (acquisition time = 8 s).

end of the applications spectrum of TCT. Figures 4(d) and 4(e) show how this technique can successfully detect blind holes 0.4, 0.6, 1, and 1.5 mm below the surface of an AISI 1010 steel block. The amplitude image Fig. 4(d) is similar to LIT. The superior probing depth of the emissivity-normalized TCT phase channel [Fig. 4(e)] in resolving the deepest defect $H4$ is evident.

In conclusion, depth-selective thermal coherence tomography has been introduced theoretically and experimentally through the utilization of temporally adjustable BPC matched filtering in diffusion-wave fields, yielding a localized response from these normally depth-integrated parabolic fields. Potential applications cover a broad spectrum, from medical diagnostics, electronic carrier waves in semiconductor junction devices, to industrial materials.

We are grateful to the Ontario Ministry of Research and Innovation (MRI) for the 2007 (inaugural) Discovery Award in Science and Engineering to A. M., the Canada Research Chairs Programs, the Federal and Provincial Governments for a CFI-ORF grant, and the Natural Sciences and Engineering Research Council of Canada for several Discovery grants to A. M.

*To whom all correspondence should be addressed.
mandelis@mie.utoronto.ca

[1] A. Mandelis, *Diffusion-Wave Fields: Green Functions and Mathematical Methods* (Springer, New York, 2001).
[2] A. Mandelis, Phys. Today **53**, No. 8, 29 (2000).
[3] M. A. O'Leary, D. A. Boas, B. Chance, and A. G. Yodh, Phys. Rev. Lett. **69**, 2658 (1992); J. A. Burt, Can. J. Phys. **64**, 1053 (1986); D. P. Almond and P. M. Patel, *Photothermal Science and Techniques* (Chapman and Hall, London, 1996); D. A. Boas, M. A. O'Leary, B. Chance, and A. G. Yodh, Phys. Rev. E **47**, R2999 (1993).
[4] J. Ordonez-Miranda and J. J. Alvarado-Gil, Int. J. Therm. Sci. **48**, 2053 (2009).
[5] A. Mandelis, L. Nicolaides, and Y. Chen, Phys. Rev. Lett. **87**, 020801 (2001).
[6] N. Levanon and E. Mozeson, *Radar Signals* (Wiley, New York, 2004), Chap. 6.
[7] H. Rohling and W. Plagge, IEEE Trans. Aerosp. Electron. Syst. **25**, 890 (1989).
[8] S. A. Prahl, A. Vitkin, and U. Bruggemann, Phys. Med. Biol. **37**, 1203 (1992).
[9] N. Tabatabaei, A. Mandelis, and B. T. Amaechi, J. Biomed. Opt. **16**, 071402 (2011).
[10] O. Breitenstein and M. LangenKamp, *Lock-In Thermography: Basics and Use for Functional Diagnostics of Electronic Components* (Springer, New York, 2003).
[11] G. M. Spirou, A. A. Oraevsky, and A. I. Vitkin, Phys. Med. Biol. **50**, N141 (2005).